

Simulation of electron transport in electron beam induced deposition of nanostructures

Francesc Salvat-Pujol, Harald O. Jeschke, Roser Valentí

Institut für Theoretische Physik, Goethe-Universität Frankfurt, Max-von-Laue-Straße 1, 60438 Frankfurt am Main, Germany

Abstract.

We present a numerical investigation of energy and charge distributions during electron-beam-induced growth of W nanostructures on SiO₂ substrates using Monte Carlo simulation of electron transport. This study gives a quantitative insight into the deposition of energy and charge in the substrate and in already existing metallic nanostructures in the presence of the electron beam. We analyze electron trajectories, inelastic mean free paths, and distribution of backscattered electrons in different deposit compositions and depths. We find that while in the early stages of the nanostructure growth a significant fraction of electron trajectories still interact with the substrate, as the nanostructure becomes thicker, the transport takes place almost exclusively in the nanostructure. In particular, a larger deposit density leads to enhanced electron backscattering. This work shows how mesoscopic radiation-transport techniques can contribute to a model which addresses the multi-scale nature of the electron-beam-induced deposition (EBID) process.

PACS numbers: 73.63.-b,81.07.-b,02.70.Uu

1. Introduction

Electron-beam-induced deposition (EBID) [1, 2, 3] is a method suitable for template-free fabrication of nanostructures. Molecules of a precursor gas are injected into a high- or ultra-high-vacuum chamber and are dissociated by a 1-50 keV focussed electron beam into a volatile fragment, which is evacuated by the vacuum system, and a non-volatile fragment, which is progressively adsorbed on a substrate, thus leading to the growth of a nanostructure at the focus of the beam. In general, the obtained deposits exhibit a granular structure consisting of nanometer-sized metal crystallites which are embedded in an insulating matrix.

There are three main interactions that determine the growth of nanostructures in the EBID process: (1) substrate-precursor interaction, (2) electron-substrate interaction and (3) electron-precursor interaction. In this work we concentrate on the electron-substrate interaction and our results have some implications for electron-precursor interaction. Existing theories for the EBID process consist mainly of equations for the deposition rate that can either be solved analytically under simplifying assumptions or in a more general form using Monte Carlo simulations. However, there is no theory which addresses the multi-scale nature of the EBID process, including microscopic and mesoscopic length and time scales, from ultra-fast (non-equilibrium processes occurring in femtoseconds) to relatively slow (growth and relaxation processes requiring nanoseconds or even microseconds).

In this work we focus on the mesoscopic length scale and present a detailed numerical study of the distribution of energy and charge originating from EBID conditions. We consider various geometric settings as well as materials relevant to EBID nanostructure growth. For our simulations we use the Monte Carlo code for radiation transport PENELOPE [4], where a statistical set of particle tracks are sampled in homogeneous materials. In this context, we provide an overview of the aspects of EBID nanostructure growth that can be studied in detail from a mesoscopic point of view using well-established radiation-transport simulation techniques for amorphous media. Recently, practical Monte Carlo simulations of EBID-nanostructure growth have been reported [15, 16], in which a plural-scattering transport model is adopted (among other approximations) whereby the inelastic scattering of electrons in solids is treated in an average fashion using the continuous slowing-down approximation. In the present work we sample inelastic interactions in detail, *i.e.*, on a per-interaction basis without employing a condensed simulation scheme, and we restrict our considerations to the interaction of the primary electrons with the substrate and the nanostructure at different stages of its growth.

The precursor gas we shall consider throughout this study is tungsten hexacarbonyl, $\text{W}(\text{CO})_6$, and the corresponding deposits $\text{W}_x\text{C}_y\text{O}_z$, *i.e.* amorphous tungsten oxycarbides with varying carbon and oxygen contents. $\text{W}(\text{CO})_6$ belongs to the class of organometallic compounds that are well established for the EBID process [5, 6, 7]. It has been studied in detail by mass spectrometry [8, 9, 10] and photoelectron or photoionization

spectroscopy [11, 12, 13], which yield appearance energies of ionic fragments as well as approximate internal energy distributions after electron ionization. The main advantage of using this precursor gas is that the tungsten metal content in the deposits can be widely varied so as to cover a wide range of electronic properties, from insulating to metallic [7, 14]. Our aim is to determine a spatially resolved picture of the growth conditions created by the electron beam within and above a SiO_2 substrate as well as within and above $\text{W}_x\text{C}_y\text{O}_z$ deposits of various thicknesses.

2. Description of the simulation

Monte Carlo simulations with PENELOPE yield tracks of primary and secondary particles on sample geometries constructed by positioning a set of well-defined homogeneous bodies in space. Random tracks are generated as follows [4]: particles are characterized by their position vector $\mathbf{r} = (x, y, z)$, energy E and a direction-of-flight unit vector $\mathbf{d} = (u, v, w)$, where u , v , and w are the direction cosines. A particle track is represented as a series of states $(\mathbf{r}_n, E_n, \mathbf{d}_n)$ where n labels the scattering event at \mathbf{r}_n leading to energy E_n and direction \mathbf{d}_n (see Figure 1). Several random variables are sampled from their respective probability distribution functions. The length of the free path to the next collision, s , is sampled from an exponential distribution with total mean free path λ_T using a random number ξ uniformly distributed in the interval $(0, 1)$,

$$s = -\lambda_T \ln \xi. \quad (1)$$

The interaction type at the new position is sampled as follows. Let us consider interactions of type A and B, with respective total cross sections σ_A and σ_B . Interactions of type A and B are sampled with probabilities

$$p_A = \frac{\sigma_A}{\sigma_T}, \quad p_B = \frac{\sigma_B}{\sigma_T}, \quad (2)$$

respectively, where $\sigma_T = \sigma_A + \sigma_B$ is the total interaction cross section. The polar scattering angle θ and the energy loss W are sampled from a distribution with azimuthal symmetry,

$$p_{A,B}(E; \theta, W) = \frac{2\pi \sin \theta}{\sigma_{A,B}(E)} \frac{d^2 \sigma_{A,B}(E; \theta, W)}{d\Omega dW}. \quad (3)$$

Finally, the azimuthal scattering angle is sampled from a uniform random number ξ as $\phi = 2\pi\xi$.

The PENELOPE code [4] uses a relatively sophisticated interaction model, devised for energies above a few hundred eV. Differential cross sections for elastic scattering were calculated with the state-of-the-art relativistic partial-wave calculation code ELSEPA [17]. Inelastic interactions are described by means of the plane-wave Born approximation using a schematized generalized-oscillator-strength model, fitted to reproduce at high energies the stopping power obtained from the asymptotic Bethe formula.

In our study it is convenient to reduce the problem to two spatial dimensions by assuming a geometry with cylindrical symmetry. We perform studies for two classes

of sample geometries: (a) a 300 nm thick layer of amorphous SiO_2 with density 2.32 g/cm^3 is placed on top of a Si wafer of density 2.33 g/cm^3 in order to study the initial conditions of the EBID growth process. We refer to this sample geometry briefly as the “substrate”. (b) Structures corresponding to intermediate EBID deposits are constructed in order to study the conditions for further growth in the EBID process, where deposited layers of different thicknesses (from 5 nm to 200 nm) are placed on top of the substrate surface, with its density and composition set in accordance with 6 different experimentally realized EBID structures [7]. While the composition in terms of atomic percent is taken from Ref. [7], the densities were determined in Ref. [14] by predicting approximate crystal structures at these given compositions using evolutionary-algorithm-based crystal structure prediction. The composition and densities of the deposits are given in Table 1. In both cases, a beam of 5-keV electrons impinges normally on the surface, with a spot size of 20 nm diameter. In practice, the electron beam is rastered on the substrate, so that the extension of the deposited nanostructure can be larger than the electron-beam spot size. Thus, a radius of 100 nm has been taken for the deposited nanostructure. Because the inelastic electron mean free path of a 5 keV electron is about 7.2 nm in Si, 6.6 nm in SiO_2 , and about 3.5 nm in the deposited structures, we set the radius of the substrate cylinder to be $1 \mu\text{m}$ in order to ensure that electrons do not leave the sample through low probability transmission events. See Figure 2 for an illustration.

Composition approximant	Density (g/cm^3)	W (at %)	C (at %)	O (at %)
$\text{WC}_{2.5}\text{O}$	7.9	22.6	56.0	21.4
$\text{WC}_{3.33}\text{O}_{0.67}$	8.7	19.0	67.1	13.8
$\text{WC}_{1.4}\text{O}_{0.8}$	9.1	31.8	44.4	23.8
$\text{WCO}_{0.71}$	10.0	36.9	35.6	27.5
$\text{WC}_{1.33}\text{O}_{0.67}$	10.4	34.0	44.3	21.7
$\text{WC}_{1.75}\text{O}_{0.75}$	10.6	27.5	50.4	22.1

Table 1. Composition of the six amorphous tungsten oxycarbide deposits considered in this study, following Ref. [7] and given in terms of atomic percent (at %). They are sorted by increasing density which was determined in Ref. [14] (see text).

Material cross sections in our calculations are approximated as an averaged weighted sum of the atomic cross sections corresponding to a given composition (incoherent sum of scattered intensities), thus neglecting chemical binding effects. Energetic electrons can scatter either elastically, where the quantum state of the scatterer remains unaltered and the direction of the projectile changes, or inelastically, where electronic excitations or ionizations take place through the different energy and momentum transfer channels available. As the electrons evolve through the medium, they lose energy in the course of several inelastic interactions. The lost energy is either absorbed by the medium through

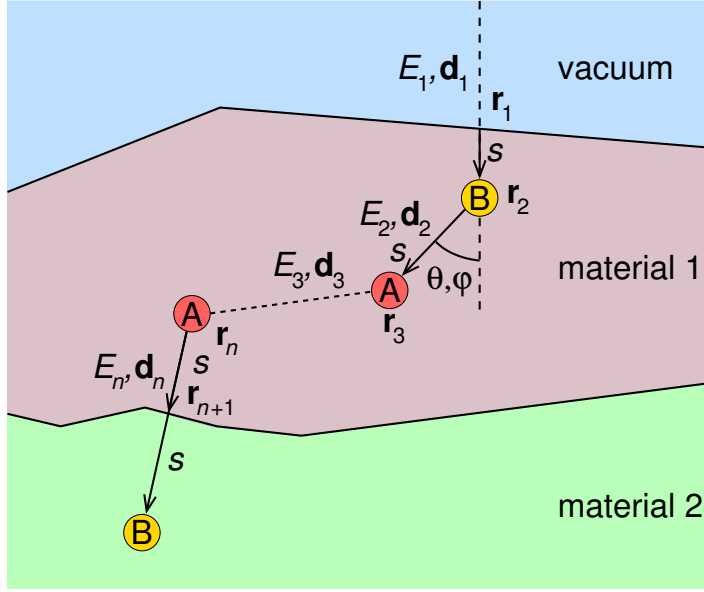


Figure 1. Schematic representation of a random trajectory generated by PENELOPE [4]. The trajectory is determined by path lengths s that determine the position \mathbf{r}_n of the next scattering event, by the type of event, and by energies E_n and directions \mathbf{d}_n after the event.

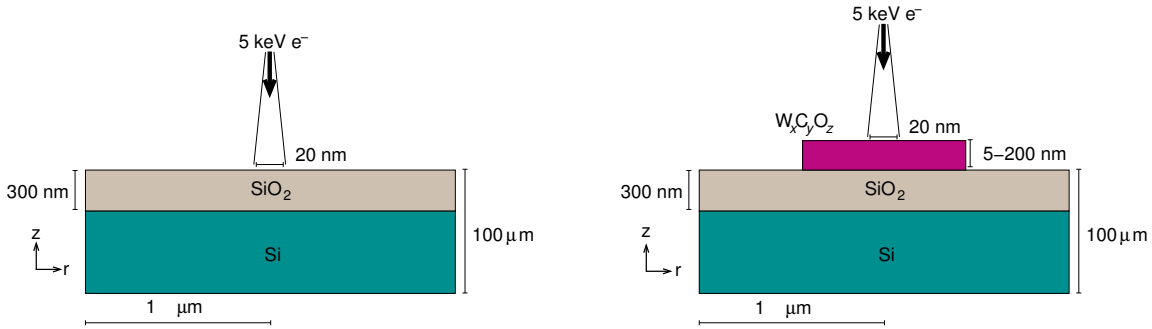


Figure 2. Cylindrical sample geometries used in the simulations. Left: A 300 nm thick amorphous SiO_2 substrate is placed above a Si wafer and irradiated with 5 keV electrons. Right: A $\text{W}_x\text{C}_y\text{O}_z$ deposit of thickness from 5 nm to 200 nm and of density and composition as given in Table 1 is placed above a 300 nm amorphous SiO_2 layer, which in turn is placed on top of a Si wafer. The electron beam of 10 nm radius is simulated by placing the source 1 cm above the center of the substrate with a beam aperture of 5.73×10^{-5} degrees and separated from the sample by vacuum. A radius of 100 nm is chosen for the deposit .

local excitations, which are allowed to relax through the emission of photons, or through ionization of the sample, which leads to the build-up of a localized positive charge in the material and to new particles, thus leading to a “shower” of particles. If an electron crosses a boundary into an adjacent material, its track history is stopped at the other side of the interface and restarted with the new material transport properties. This can be done any time, since electron trajectories are modelled as Markov processes (the future of the trajectory is dependent only on the present state, and not on the past).

The track history of an electron is stopped when its energy drops below 50 eV: the electron is then considered absorbed by the medium, contributing to the build-up of a localized negative charge in the material. We choose an absorption energy of 50 eV because we are neglecting binding effects in the material, and furthermore, elastic and inelastic cross sections derived from atomistic models carry large uncertainties already for energies below a few hundred eV.

3. Results

To provide a first visual insight into the electron transport process in the substrate and in the deposited nanostructure, Figure 3 displays a simulated shower of 5-keV-electron trajectories impinging normally on a 500 nm thick slab of SiO₂ (left-hand side, substrate material) and pure W (right-hand side, deposit material), respectively. We consider pure tungsten as a representative material of the different deposits for practical reasons. This choice is reasonable inasmuch as the average distance between consecutive inelastic collisions [inelastic mean free path (IMFP)] of electrons in W and in the considered nanostructure materials are very similar in the energy window of interest (see Figure 4). Note, that in the SiO₂ substrate the beam is completely attenuated at a depth of ~ 500 nm, whereas in W this depth is reduced to ~ 150 nm. Indeed, the IMFP of electrons in SiO₂ is roughly a factor 2–4 larger than the IMFP of electrons in W (or any of the 6 considered deposit materials), as shown on the left-hand panel of Figure 4. On the right-hand panel of Figure 4 we also include the average distance between consecutive elastic interactions for completeness. Thus, we conclude that in the early stages of the nanostructure growth (thicknesses much smaller than ~ 150 nm), the electron beam probes both the thin deposit and the substrate. The energy and charge deposition processes are therefore dictated by the transport characteristics of both the deposit and the substrate. On the other hand, for nanostructure thicknesses exceeding ~ 150 nm, the deposition of energy and charge takes place almost exclusively in the nanostructure, without affecting the substrate.

Figure 5(a) displays the energy distribution of electrons backscattered and emitted per incoming electron from the substrate (darkest curve) and from deposits of increasing thicknesses d_{WCO} on top of the substrate [dark blue curve, $d_{\text{WCO}} = 5$ nm, through light blue curve, $d_{\text{WCO}} = 200$ nm]. Notice that for thin deposits the spectral features of the substrate are merely smeared out, owing to the fact that only few inelastic interactions take place in the thin deposit. For increasing deposit thicknesses, the transport in the substrate plays an increasingly marginal role. Thus, for thick deposits the spectral features of the substrate vanish and the spectral features of the deposit prevail. This explains the saturated behavior of the curves corresponding to $d_{\text{WCO}} = 100$ nm and $d_{\text{WCO}} = 200$ nm, where electrons are very unlikely to even reach the substrate, in accordance with the discussion of Figure 3. It is interesting to note that the intensity in the energy distribution of backscattered electrons increases with the sample thickness. Indeed, on the one hand the elastic backscattering coefficient increases with the atomic

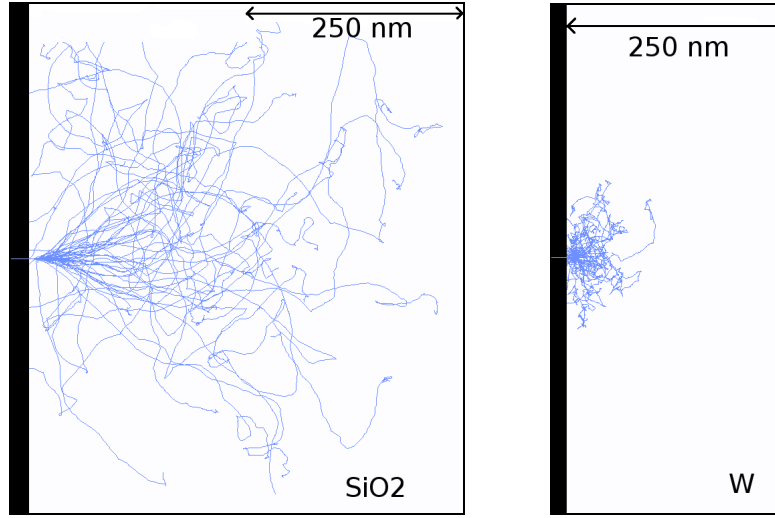


Figure 3. Snapshot of 50 simulated electron trajectories in nanostructure deposit material W (left-hand side, representative for material deposit) and in the SiO_2 substrate (right-hand side). The width of the screenshot windows corresponds to 500 nm.

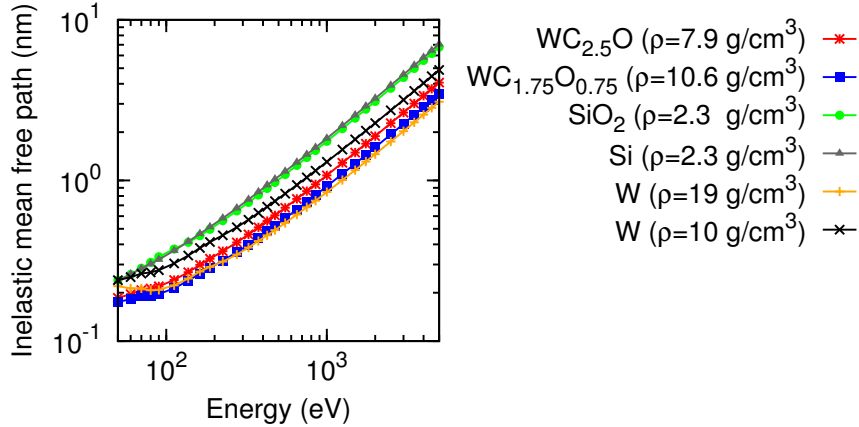


Figure 4. Inelastic mean free paths for the relevant materials in this work presented in the usual log-log scale. The tungsten oxycarbide compositions $\text{WC}_{2.5}\text{O}$ and $\text{WC}_{1.75}\text{O}_{0.75}$ correspond to the lowest and highest density samples of Table 1, respectively.

number, leading to the observed increase in the elastic peak at 5 keV [the substrate consists of Si and O (atomic numbers $Z = 14$ and $Z = 8$, respectively) whereas the deposit material contains W ($Z = 74$)]. On the other hand, the IMFP is inversely proportional to the material density, so that a denser deposit on a comparatively light substrate implies an increase in the number of energy losses per unit path length with respect to those that would take place in the substrate alone. This justifies the factor ~ 2 between the curves corresponding to the (thick) deposit and the substrate. Thus, under the assumption that the presence of a large number of electrons (slow or fast) enhances the dissociation rate of precursor gas molecules adsorbed on the substrate,

one can infer the following positive-feedback process: as the deposit thickness grows, so does the number of backscattered and emitted electrons, leading to an improvement in the dissociation rate and, therefore, in the nanostructure deposition rate, leading to a reinforced growth process.

Two aspects of Figure 5(a) should be emphasized. (1) In order to further elucidate the dependence of the electron backscattering probability with the atomic number of the deposit material, the simulation was repeated replacing the deposit with Co, a comparatively lighter material ($Z = 27$). Figure 5(b) displays the energy distribution of backscattered electrons for different Co-nanodeposit thicknesses, d_{Co} . Notice that the increase in the elastic-peak intensity is roughly a factor 2 or 3 smaller than for the nanostructure material, which is much heavier. (2) Notice that as the deposit becomes thicker, the intensity of the curves increases monotonically, reaching its maximum for a thickness of about 50 nm and then decreasing slightly into its saturated value for thicknesses of 200 nm. The fact that multiple elastic and inelastic interactions take place along the trajectory makes it hard to give a detailed explanation of this effect. Nevertheless, it can be argued that for thicknesses exceeding 50 nm, the fraction of trajectories which reach the substrate becomes negligible and, for thick enough deposits, this fraction approaches zero. Owing to the fact that the mean free paths in the deposit are much shorter than in the substrate, more energy losses take place per unit path length in the deposit than in the substrate. This implies that the thicker the deposit becomes, the larger is the number of electrons which leave the sample after losing most of its energy. This explains, at least qualitatively, the increase and eventual saturation in the low-energy regime of the spectrum (contribution of electrons which leave the sample after losing most of its energy and of emitted secondary electrons), as well as the decrease in intensity in the energy range between 1 and 4 keV (for thick substrate electrons in this regime lose more energy and therefore the spectral intensity shifts to lower energies). Close to the elastic peak, variations with the thickness of the substrate between 50 nm and 200 nm are not visible, since the elastic backscattering probability for the deposit is much larger than for the substrate.

The primary energy of the electrons (5 keV) is high enough to produce inner-shell ionizations in Si and O. Let S_0 denote the ionized shell. A second electron from an outer shell, S_1 , fills the vacancy and, subsequently, two processes are possible: (1) a radiative transition whereby a photon is emitted with a characteristic energy $U_{S_0} - U_{S_1}$, where U denotes the ionization energy of the corresponding shell, or (2), typically more likely, a non-radiative transition whereby an electron from an outer shell S_2 (which can either coincide with or be less bound than S_1) is emitted as an Auger electron with energy $U_{S_0} - U_{S_1} - U_{S_2}$. The emitted photons might either leave the sample or be absorbed by a target atom, leading to photoelectron emission. Figure 6 displays the distribution of electrons (solid red curve) and photons (dashed blue curve) emitted from the substrate per incoming electron in the absence of a deposit. The peaks in the photon spectrum, superimposed on a bremsstrahlung background, correspond to K lines of Si and O, situated at 1739–1835 eV and 523 eV, respectively. Notice that the

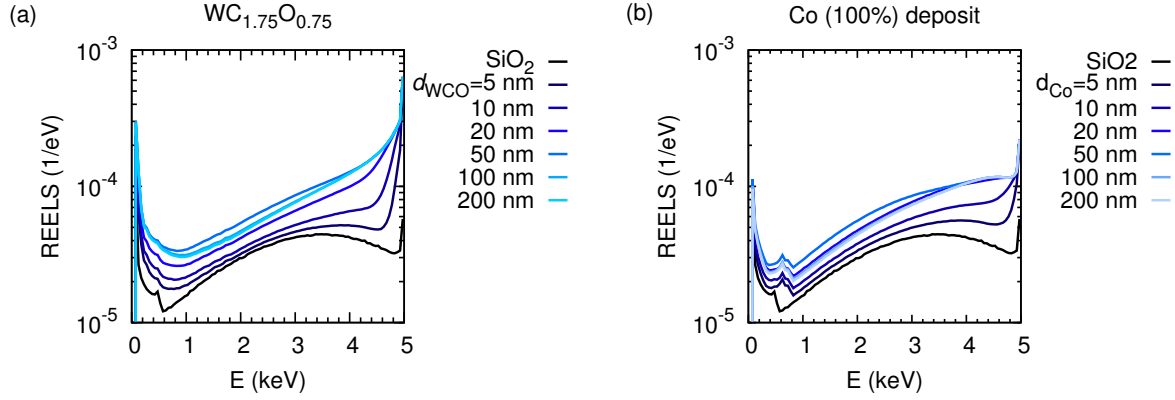


Figure 5. (a) Distribution of electrons backscattered and emitted into the vacuum from the substrate in absence of a deposit (black curve) and from the substrate with a deposit of thickness d_{WCO} ranging from 5 nm to 200 nm (rest of curves) consisting of the material corresponding to the composition $WC_{1.75}O_{0.75}$ (see Table 1). (b) Same as panel (a) for a deposit of pure Co. Notice that the ordinates are in a logarithmic scale, whereas the abscissas are in a linear scale. The acronym REELS stands for reflection electron-energy-loss spectrum.

number of photons emitted per incoming electron is at least two orders of magnitude smaller than the number of emitted electrons. Furthermore, interaction mean free paths for photons are typically much longer than for electrons. Thus, the contribution of the emitted photons to the energy and charge deposition processes is presumably negligible, except for the minor photoelectron peak in the electron spectrum of the substrate at 500 eV, superimposed to a contribution from Auger electron emission from O with energies from 478.8 eV to 508.9 eV. A contribution of Auger- or photoelectrons is not observed at 1739–1835 eV, because (1) Auger-electron energies are spread over a few hundred eV and thus do not lead to a well resolved peak and (2) the photoelectric cross section at these energies one order of magnitude smaller than at 500 eV (cross section data taken from the numerical database of PENELOPE [4]). The photon spectrum was also examined when a deposit lies on the substrate without finding significant deviations regarding the minor role played by photon transport as demonstrated for the pure substrate.

Figure 7 displays the distribution of energy deposited in the system as a function of depth for sample thicknesses d_{WCO} ranging from 10 nm to 200 nm. Negative depths correspond to the SiO_2 substrate, whereas positive depths denote the deposit, indicated respectively by the magenta and grey bars (reflecting the color code in Figure 2). The black solid and the dashed red curve correspond to $WC_{2.5}O$ (lowest density sample) and $WC_{1.75}O_{0.75}$ (highest density sample), respectively. The panel corresponding to $d_{WCO} = 200$ nm additionally shows the deposited energy for samples with intermediate values of the density. It is clear that the deposited energy per unit depth is much higher in the deposit than in the substrate, since the IMFP is a factor ~ 2 shorter in the deposit than in the substrate, and thus energy-loss events take place more often in the deposit than in the substrate. This also explains the discontinuous jump at the

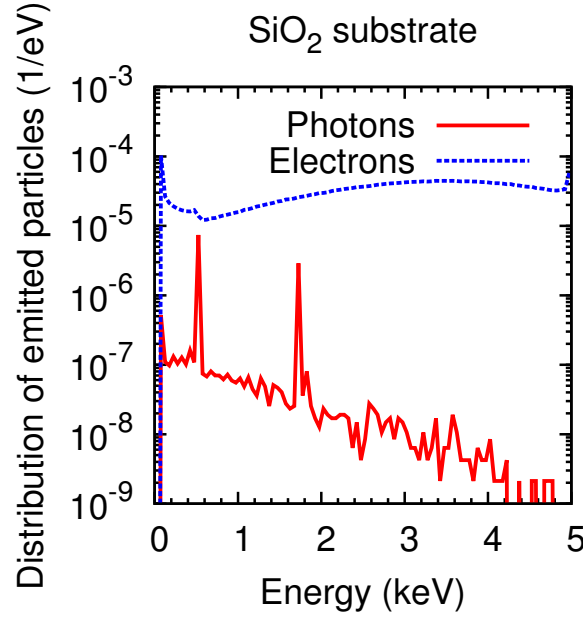


Figure 6. Distribution of electrons backscattered and emitted into the vacuum from the substrate in the absence of a deposit (dashed curve) and distribution of photons emitted into the vacuum (solid curve). Note, that the ordinates are in a logarithmic scale, whereas the abscissas are in a linear scale.

deposit-substrate interface.

It should be noted that, whereas the density increases linearly from $\text{WC}_{2.5}\text{O}$ to $\text{WC}_{1.75}\text{O}_{0.75}$, the tungsten content does not exhibit a clear trend (see Table 1). In order to separately exhibit the effect of density and W-content variations on the distribution of deposited energy, we have considered the following artificial material variations. On the one hand, we have taken a sample with a fixed density $\rho = 10.6092 \text{ g/cm}^3$ (corresponding to $\text{WC}_{1.75}\text{O}_{0.75}$) and have varied its W content from 17.5% to 37.5% in steps of 2.5% (covering the range of W contents in Table 1), decreasing both the C and the O contents by 1.25% at each step. We have also considered the extreme case of 100% W content. The distribution of deposited energy as a function of depth is shown in Figure 8 and the corresponding IMFPs are displayed in Figure 9. On the other hand, we have taken a sample with a fixed W content (27.5% W, 50.4% C, 22.1% O, corresponding to $\text{WC}_{1.75}\text{O}_{0.75}$) and have varied its density from 8 g/cm^3 to 12 g/cm^3 (covering the range of densities given in Table 1). The distribution of deposited energy and the corresponding IMFPs are shown in Figures 10 and 11, respectively. Comparing Figures 8 and 10 we conclude that variations in the density influence the energy deposition process in the nanostructure much more strongly than variations in the W content (in the considered variation intervals of these parameters). This can be best observed in the case of sample thickness $d_{\text{WCO}} = 200 \text{ nm}$ for $z = 50$ to 150 nm .

In practice, sample charging effects in the EBID process cause only a minor repulsion of the electron beam (observed as a slight drift in the monitoring images) which can be easily corrected by applying appropriate beam-deflection voltages. Nevertheless

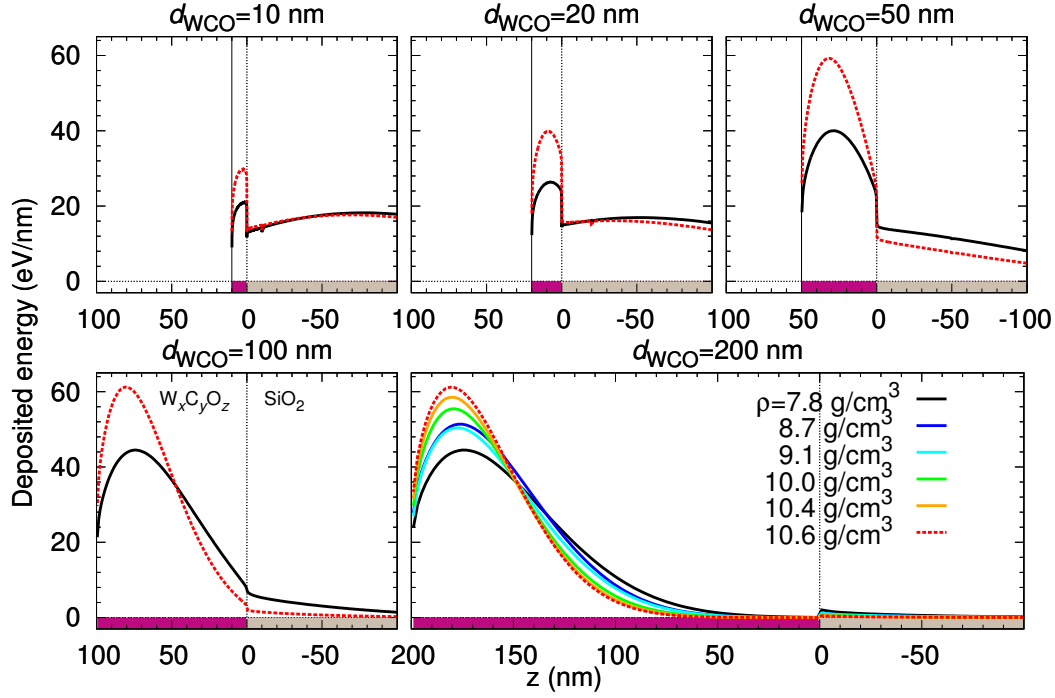


Figure 7. Energy deposited in the system as a function of the depth z for the indicated sample thicknesses d_{WCO} and for the six nanostructure materials specified in Table 1. The position $z = 0$ corresponds to the deposit-substrate interface; the position $z = d_{\text{WCO}}$ (indicated by a solid vertical line in the three upper panels) corresponds to the deposit-vacuum interface. Notice that, in addition to the density, the composition of the samples varies (see Table 1).

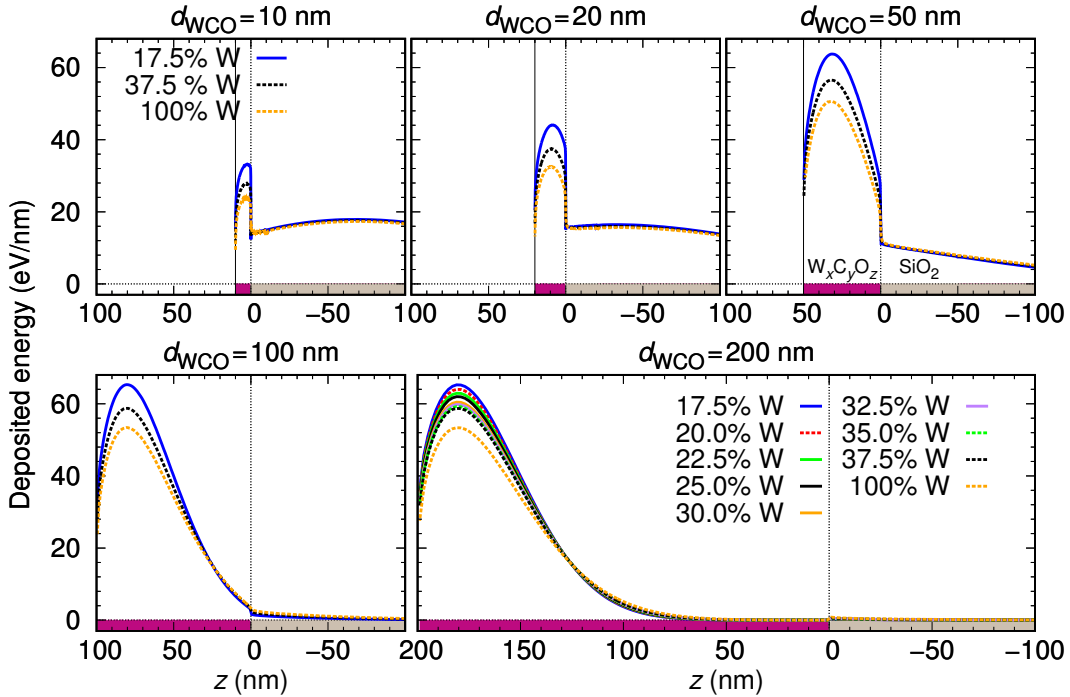


Figure 8. Same as Figure 7 for a fixed deposit density ($\rho = 10.6092$ g/cm³) and variable tungsten content.

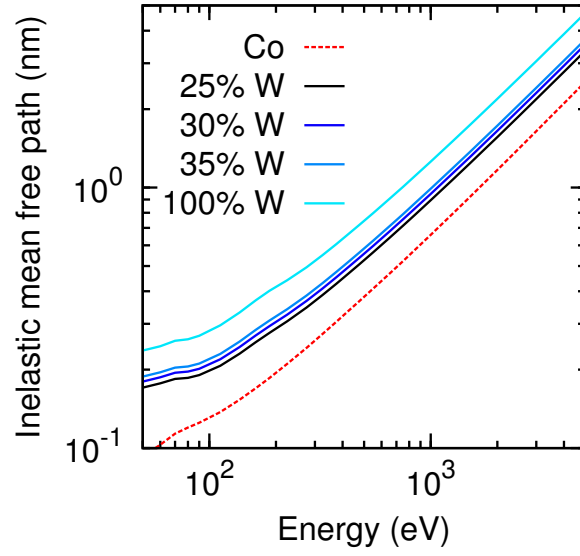


Figure 9. IMFP in the different deposits with fixed density ($\rho = 10.6092 \text{ g/cm}^3$) and variable tungsten content.

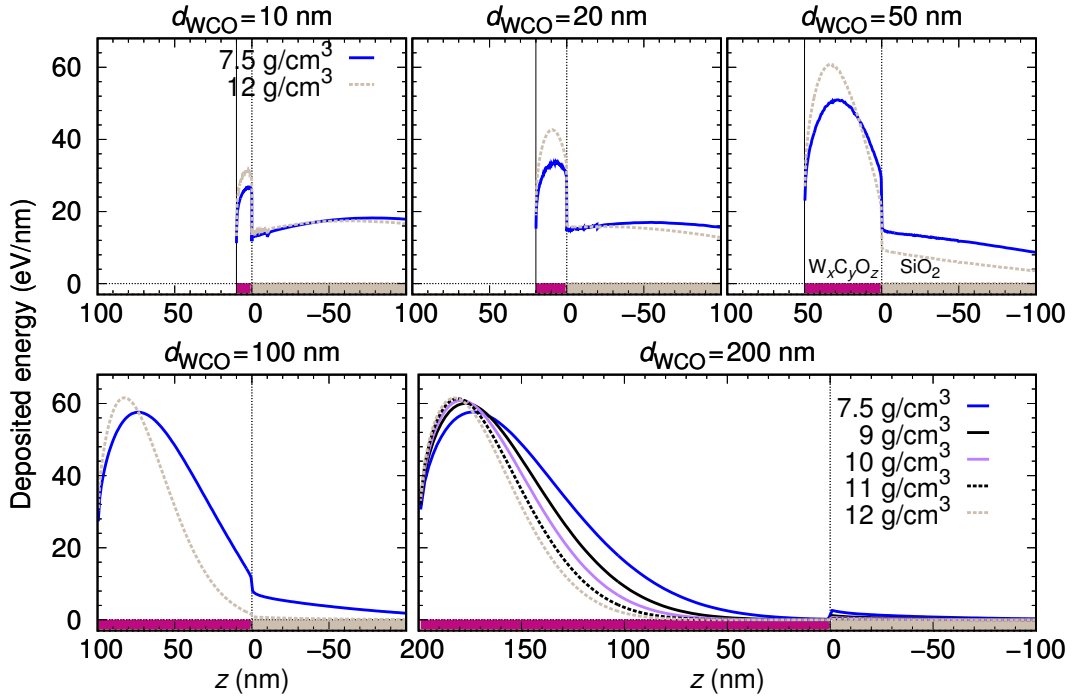


Figure 10. Same as Figure 7 for a fixed composition (27.5% W, 50.4% C, 22.1% O) and variable density.

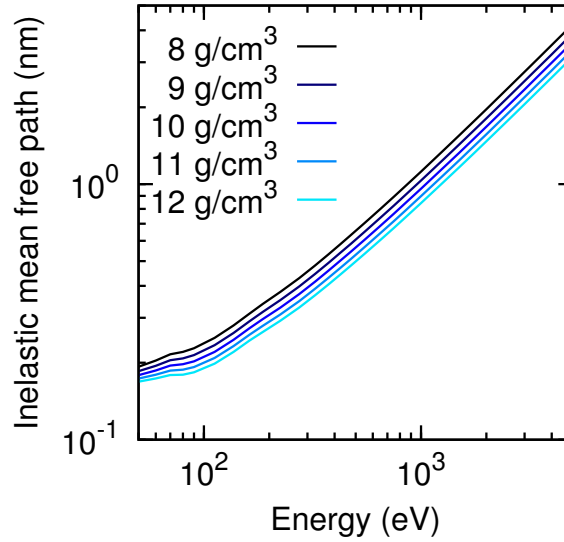


Figure 11. IMFP in different deposits with fixed composition (27.5% W, 50.4% C, 22.1% O) and variable density.

it is interesting *per se* to examine the spatial distribution of the charge deposition process induced by the incoming beam, if only to better delimit the spatial region that is probed and affected by the beam. Figure 12 displays the distribution of charge deposited per unit path length for deposit thicknesses d_{WCO} ranging from 10 nm to 200 nm in $\text{WC}_{2.5}\text{O}$ and $\text{WC}_{1.75}\text{O}_{0.75}$ (solid black and dashed red line, respectively). Calculations were also carried out for samples of intermediate densities but are not shown in the Figure, which displays only the two extreme cases for clarity. Note, that the charge deposited in the nanostructure close to the vacuum interface is positive. This implies that there are more secondary electrons emitted from this region than slow electrons absorbed in it. Indeed, those secondary electrons emitted from the nanostructure into the vacuum do not return, implying that close to the vacuum interface it is more likely to see a lack of electrons than the absorption of slow electrons. Deeper into the nanostructure, the absorption of slow electrons becomes more likely: secondary electrons are more likely to become absorbed than to reach the interface into vacuum. This leads to the observed decrease in the deposited charge, which becomes even negative when the nanostructure is thick enough so that all generated secondary electrons are eventually absorbed in it. Regarding the deposit-substrate interface, two aspects should be considered. On the one hand, the primary electron loses less energy in the SiO_2 substrate than in the nanostructure material, so that less secondary electrons are generated per unit path length in the substrate. On the other hand, secondary electrons from the nanostructure cross the interface into the substrate. The number of slow electrons moving from the nanostructure into the substrate is larger than the number of slow electrons moving in the opposite direction. This leads to the observed increase in positive (negative) charge in the nanostructure (substrate) side of the interface.

Finally, Figures 13 and 14 display, respectively, the distribution of deposited energy

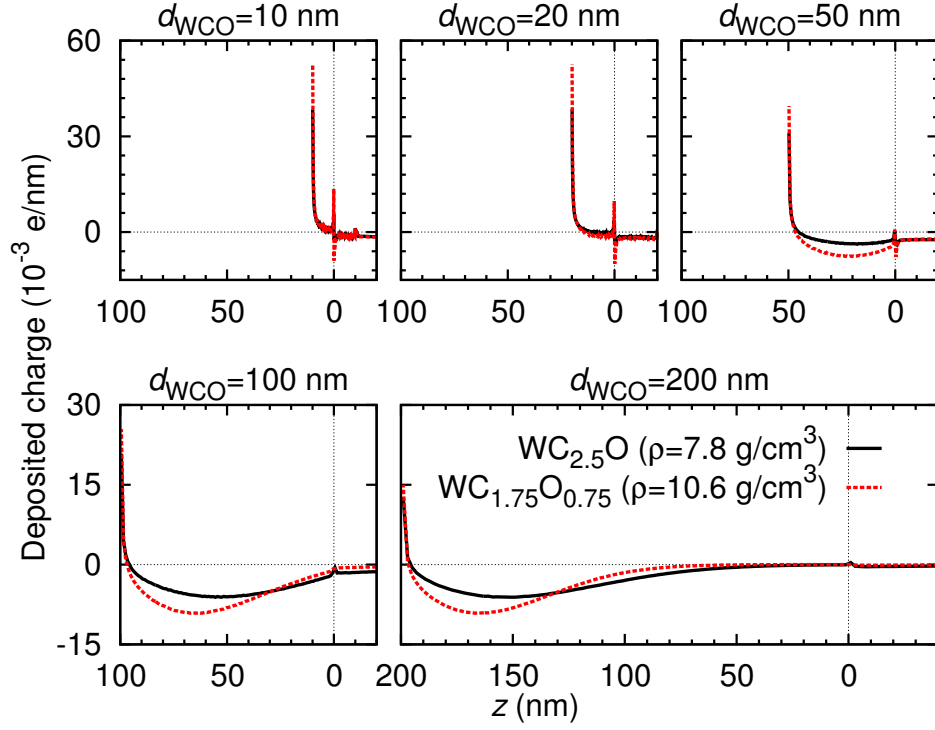


Figure 12. Charge deposited into the system as a function of the depth z for the indicated sample thicknesses d_{WCO} and for the six nanostructure materials specified in Table 1 (compare with Figure 7).

and charge as a function of the depth and the radial coordinate in $\text{WC}_{1.75}\text{O}_{0.75}$ (highest density sample) for nanostructure thicknesses of 10 and 100 nm. The panels in the right-hand side show cross sections of the distributions at the indicated depths z . In these figures one can clearly identify the beam radius of 10 nm. Notice that at radii $r < 10 \text{ nm}$ the deposited charge is positive. In this region, secondary electrons are emitted as a result of the energy loss of the primary electrons. For distances $r > 10 \text{ nm}$, the deposited charge is negative, meaning that electrons with $E \leq 50 \text{ eV}$ are absorbed there. These slow electrons are those secondary electrons generated in $r < 10 \text{ nm}$ which wander into $r > 10 \text{ nm}$ and are not able to travel further, being absorbed.

The distribution of deposited energy as a function of the depth and of the radial coordinate has additional value. On the one hand, it can be used to derive a temperature distribution for more detailed microscopic simulations (*e.g.* molecular dynamics) of the EBID process. On the other hand, the deposited energy also contributes to an enhancement of the dissociation of precursor gas molecules adsorbed on the surface, and thus contributes to a well-sustained nanostructure growth. It is therefore worthwhile to have an accurate estimate for this quantity.

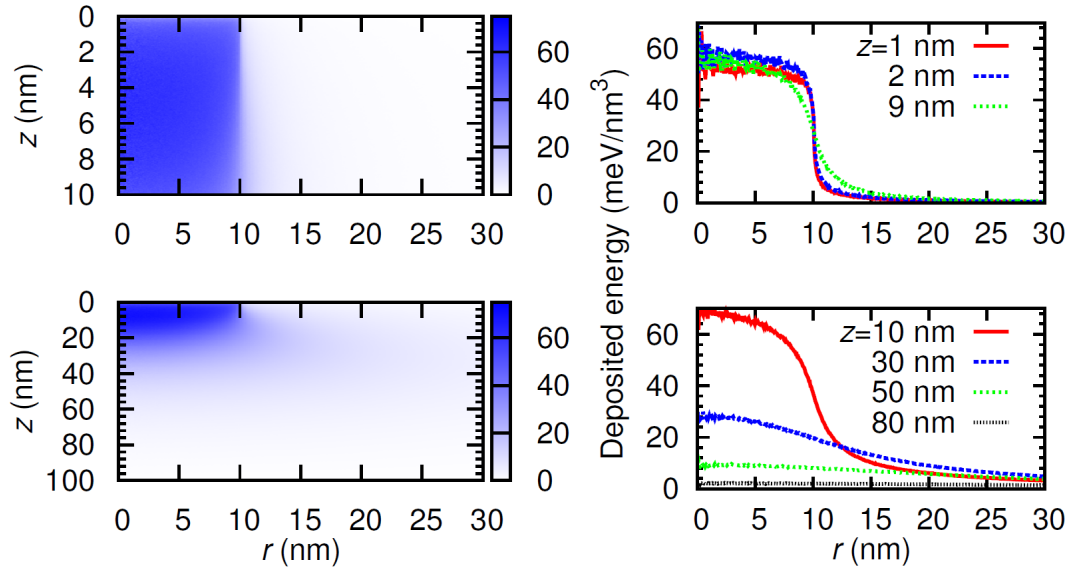


Figure 13. Distribution of energy deposited in $\text{WC}_{1.75}\text{O}_{0.75}$ as a function of the depth z and the radial coordinate r . The two upper (lower) panels correspond to a sample thickness $d_{\text{WCO}} = 10$ nm ($d_{\text{WCO}} = 100$ nm). The right-hand-side panels display cross sections of the distribution at the indicated depths z below the deposit-vacuum interface.

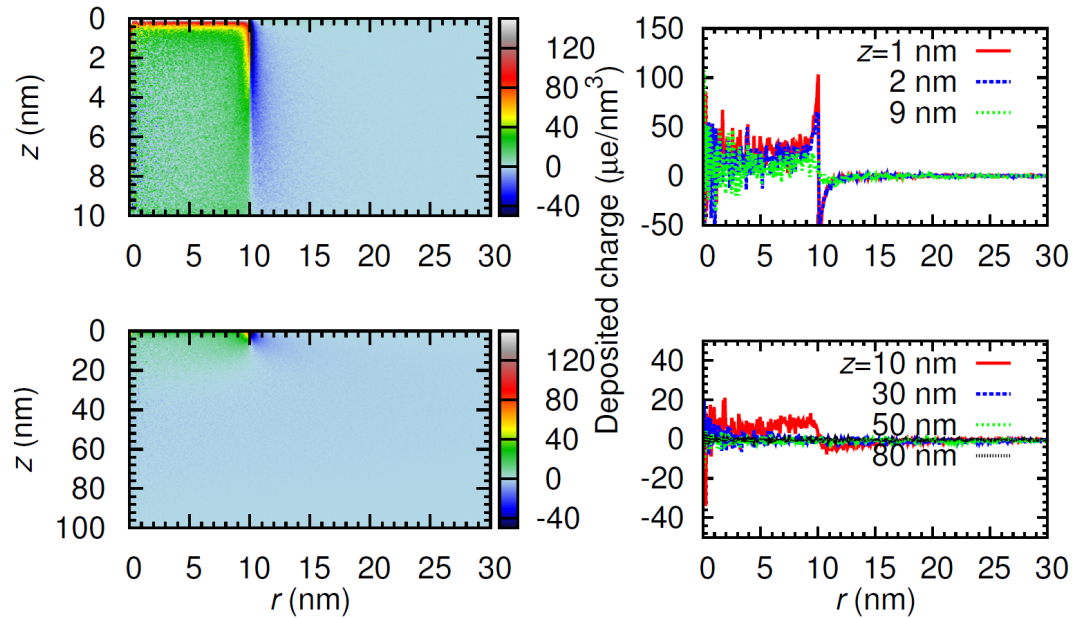


Figure 14. Same as Figure 13 for the charge deposited in $\text{WC}_{1.75}\text{O}_{0.75}$.

4. Conclusions

In this work we presented results of Monte Carlo simulations of electron transport which provide valuable insight into the charge and energy deposition processes induced by the primary electron beam in the EBID process of $\text{W}(\text{CO})_6$ nanostructures on SiO_2 substrates. The simulations highlight the differences in the transport of electrons in the nanostructure and in the substrate: the mean free path between consecutive inelastic interactions in the deposit is a factor ~ 2 smaller than in the substrate which leads to a beam attenuation after a depth of ~ 500 nm in the substrate material, whereas, in the nanostructure material, the beam is attenuated at much shallower depths of ~ 150 nm. In the early stages of the nanostructure growth (thickness well below 150 nm), a significant fraction of incoming electron trajectories still interact with the substrate. As the nanostructure becomes thicker ($\gtrsim 100$ nm), the transport takes place almost exclusively in the nanostructure, leading to a saturated behavior of the distribution of the deposited energy, charge, and backscattered electrons. The simulations show two effects which may be important for the growth of the nanostructure. (1) The energy deposited in the substrate is available for the dissociation of precursor-gas molecules adsorbed on the surface substrate. (2) If we assume that a larger yield of secondary electrons enhances precursor dissociation and improves the conditions for nanodeposit growth with high density and metal content, then the simulations show that larger deposit density leads to enhanced electron backscattering. This implies that random fluctuations in deposit density could be amplified through positive feedback.

The presented simulations therefore provide an overview of the effect of the primary-electron beam on the deposit and on the substrate at different stages of the nanostructure growth. Furthermore, the distributions of deposited energy serve as a starting point for further microscopic simulations (molecular dynamics) in that they provide a guideline for the initial temperature distribution in the substrate and the deposit under irradiation with an electron beam.

Acknowledgments

We are indebted to Prof. Francesc Salvat of the Universitat de Barcelona for the very fruitful discussions and we acknowledge the contribution of Carlos Ortiz at the beginning of this work. Funding by the Beilstein-Institut is gratefully acknowledged. This work was supported by the Helmholtz Association (HA216/EMMI).

- [1] Koops H, Kretz J, Rudolph M and Weber M 1993 Constructive 3-dimensional lithography with electron-beam-induced deposition for quantum effect devices *J. Vac. Sci. Technol. B* **11** 2386
- [2] Randolph S, Fowlkes J and Rack P 2006 Focused, nanoscale electron-beam-induced deposition and etching *Critical Reviews in Solid State and Materials Sciences* **31** 55
- [3] Utke I, Hoffmann P and Melngailis J 2008 Gas-assisted focused electron beam and ion beam processing and fabrication *J. Vac. Sci. Technol. B* **26** 1197
- [4] Salvat F, Fernandez-Varea J, Acosta E and Sempau J 2011 PENELOPE-2001: A Code System for Monte Carlo Simulation of Electron and Photon Transport *NEA - Nuclear Energy Agency*
- [5] Hoyle P, Ogasawara M, Cleaver J and Ahmed H 1993 Electrical resistance of electron-beam-induced deposits from tungsten hexacarbonyl *Applied Physics Letters* **62** 3043
- [6] Hoyle P., Cleaver J. and Ahmed H. 1996 Electron beam induced deposition from $W(CO)_6$ at 2 to 20 keV and its applications *J. Vac. Sci. Technol. B* **14** 662
- [7] Huth M., Klingenberg D., Grimm C., Poratti F. and Sachser R. 2009 Conductance regimes of W-based granular metals prepared by electron beam induced deposition *New Journal of Physics* **11** 033032
- [8] Beranová S. and Wesdemiotis C. 1994 Internal energy-distributions of tungsten hexacarbonyl ions after neutralization-reionization *Journal of the American Society for Mass Spectrometry* **5** 1093
- [9] Cooks R., Ast T., Kralj B., Kramer V. and Zigon D. 1990 Internal energy-distributions deposited in doubly and singly charged tungsten hexacarbonyl ions generated by charge stripping, electron-impact, and charge-exchange *Journal of the American Society for Mass Spectrometry* **1** 16
- [10] Michels G., Flesch G. and Svec H. 1980 Comparative mass-spectrometry of the group-6b hexacarbonyls and pentacarbonyl thiocarbonyls *Inorganic Chemistry* **19** 479
- [11] Cooper G., Green J., Payne M., Dobson B. and Hillier I. 1987 Photoelectron-spectroscopy with variable photon energy - a study of the metal hexacarbonyls, $W(CO)_6$, $Cr(CO)_6$, $Mo(CO)_6$ *Journal of the American Chemical Society* **109** 3836
- [12] Hubbard J. and Lichtenberger D. 1982 Vibrational fine-structure in the valence ionizations of transition-metal hexacarbonyls - new experimental indication of metal-to-carbonyl pi-bonding *Journal of the American Chemical Society* **104** 2132.
- [13] Qi F., Yang S., Sheng L., Gao H., Zhang Y. and Yu S. 1997 Vacuum ultraviolet photoionization and dissociative photoionization of $W(CO)_6$ *J. Chem. Phys.* **107** 10391
- [14] Muthukumar K., Valentí R. and Jeschke H. O. 2012 Simulation of structural and electronic properties of amorphous tungsten oxycarbides *New J. Phys* **14** 113028
- [15] Smith D.A., Fowlkes J.D. and Rack P.D. 2007 A nanoscale three-dimensional Monte Carlo simulation of electron-beam-induced deposition with gas dynamics *Nanotechnology* **18** 265308
- [16] Smith D.A., Fowlkes J.D. and Rack P.D. 2008 Understanding the Kinetics and Nanoscale Morphology of Electron-Beam-Induced Deposition via a Three-Dimensional Monte Carlo Simulation: The Effects of the Precursor Molecule and the Deposited Material *Small* **4** 1382
- [17] Salvat F., Jablonski A. and Powell C.J. 2005 ELSEPA - Dirac partial-wave calculation of elastic scattering of electrons and positrons by atoms, positive ions and molecules *Comput. Phys. Commun.* **165** 157.